

Forecasting Continuum Intensity for Solar Active Region Emergence Prediction using Transformers

Jonas Tirona¹, Sarang Patil¹, Spiridon Kasapis², Eren Dogan¹, John Stefan¹,
Irina N. Kitiashvili³, Alexander G. Kosovichev^{1,3}, Mengjia Xu¹

¹New Jersey Institute of Technology, Newark, NJ, USA

²Princeton University, Princeton, NJ, USA

³NASA Ames Research Center, Moffett Field, CA, USA

Abstract

Early and accurate prediction of solar active region (AR) emergence is crucial for space weather forecasting. Building on established Long Short-Term Memory (LSTM) based approaches for forecasting the continuum intensity decrease associated with AR emergence, this work expands the modeling with new architectures and targets. We investigate a sliding-window Transformer architecture to forecast continuum intensity evolution up to 12 hours ahead using data from 46 ARs observed by SDO/HMI. We conduct a systematic ablation study to evaluate two key components: (1) the inclusion of a temporal 1D convolutional (Conv1D) front-end and (2) a novel ‘Early Detection’ architecture featuring attention biases and a timing-aware loss function. Our best-performing model, combining the Early Detection architecture without the Conv1D layer, achieved a Root Mean Square Error (RMSE) of 0.1189 (representing a 10.6% improvement over the LSTM baseline) and an average advance warning time of 4.73 hours (timing difference of -4.73h), even under a stricter emergence criterion than previous studies. While the Transformer demonstrates superior aggregate timing and accuracy, we note that this high-sensitivity detection comes with increased variance compared to smoother baseline models. However, this volatility is a necessary trade-off for operational warning systems: the model’s ability to detect micro-changes in precursor signals enables significantly earlier detection, outweighing the cost of increased noise. Our results demonstrate that Transformer architectures modified with early detection biases, when used without temporal smoothing layers, provide a high-sensitivity alternative for forecasting AR emergence that prioritizes advance warning over statistical smoothness.

Plain Language Summary

Solar active regions are areas of intense magnetic flux on the Sun that drive space weather events, such as solar flares, which can disrupt technologies on Earth. Forecasting the emergence of these regions is challenging because the warning signs, subtle variations in the Sun’s acoustic and magnetic patterns, are faint and difficult to detect before the region becomes visible. In this study, we applied a Transformer machine learning architecture, designed to recognize complex sequential patterns, to analyze these precursor signals to predict the emergence of solar active regions. We compared standard models against a specialized “Early Detection” architecture. We found that standard architectures often prioritize statistical stability, and the addition of convolutional layers effectively smooth out the faint data spikes that signal the start of an event, causing inaccuracies in timing prediction. By modifying the model to be more sensitive to these initial fluctuations, our approach successfully predicted the emergence of active regions approximately 5 hours in advance. This demonstrates that for operational space weather forecasting, models must be designed to prioritize early detection of faint signals rather than prioritizing the smoothness of the prediction.

1 Introduction

Solar active regions (ARs) manifest from the Sun’s magnetic field emerging from the convection zone to the photosphere (e.g., van Driel-Gesztelyi & Green, 2015), from where they drive events like space weather conditions by producing space weather events such as solar flares (e.g., Schrijver, 2009), coronal mass ejections (CMEs; e.g., Howard et al., 1985) and Solar Energetic Particles (SEPs; e.g., Whitman et al., 2023). These events, if sufficiently intense, can inject energetic particles in Earth’s magnetosphere and affect technological infrastructure (e.g. Horne et al., 2013; Kasapis, Thompson, et al., 2023; Pak et al., 2025). Therefore, understanding when ARs emerge on the photosphere and produce flares, CMEs, and SEPs is crucial for predicting such geoeffective space-weather events and mitigating their effects on space-based infrastructure.

The emergence process of ARs involves rising magnetic flux through the solar interior, producing observable signatures in helioseismic data hours to days before becoming visible as sunspots (A. Kosovichev et al., 2001; Ilonidis et al., 2011; Stefan & Kosovichev, 2023). A number of helioseismic studies have confirmed that variations in the travel times of interior-penetrating acoustic waves can signal the upcoming flux emergence that later will form in ARs, before it can be observed visually on the photosphere (e.g., Birch et al., 2012; Leka et al., 2013; Barnes et al., 2014; Stefan & Kosovichev, 2023). These travel time variations are extracted through Fourier and cross-correlation analyses of the surface velocity field, and it has been recently shown that direct use of the velocity field—without the use of computationally-expensive helioseismic inversion techniques—can also be effective in retrieving information about subsurface emerging magnetic flux (Kasapis, Kitiashvili, et al., 2025), (Keegan et al., 2025). Recently, advances in machine learning and helioseismology have shown promise for predicting AR emergence using time-series analysis of solar oscillations observed on the solar surface (A. G. Kosovichev et al., 2025).

An initial architecture for studying such temporal sequence modeling was the Long Short-Term Memory (LSTM) network (Kasapis, Kitiashvili, et al., 2023), originally introduced by Hochreiter & Schmidhuber (1997). Designed to mitigate the vanishing gradient problem inherent in standard Recurrent Neural Networks (RNNs), LSTMs utilize a gating mechanism to regulate the flow of information, making them particularly effective for learning order-dependence in time-series data. Kasapis, Kitiashvili, et al. (2023, 2025) demonstrated that LSTMs could successfully forecast the continuum intensity associated with AR emergence by analyzing acoustic power and magnetic flux variations derived from the Helioseismic and Magnetic Imager (HMI) instrument data (Scherrer et al., 2012; Hoeksema et al., 2014) onboard the Solar Dynamics Observatory (SDO) (Pesnell et al., 2012), achieving predictions 10-29 hours in advance for several test cases. However, LSTMs are not immune to the limitations of recurrent architectures. Their sequential processing nature requires information to traverse every intermediate time step, which can cause the backpropagated error gradients—the signals used to update model weights—to diminish over extended sequences. This attenuation effectively prevents the model from learning relationships between distant time points.

To address these limitations and capture complex temporal dynamics more effectively, Transformer architectures (Vaswani et al., 2017) have revolutionized sequence modeling across multiple domains through their self-attention mechanisms, which enable direct modeling of relationships between any two positions in a sequence regardless of their temporal distance. In time-series forecasting applications, Transformers have demonstrated superior performance over recurrent models by effectively capturing both local patterns and global dependencies (e.g., Zhou et al., 2021; Wu et al., 2021). For solar physics applications, the ability to simultaneously analyze multiple temporal scales may prove particularly valuable given the multi-scale nature of the Sun's magnetic activity.

This work extends the developments of predicting AR emergence by investigating the optimal architecture for a sliding-window Transformer. We present the first application of Transformer architectures to predict continuum intensity evolution driven by active region emergence. We conduct a systematic ablation study to evaluate two key components of our proposed forecasting framework: (1) the inclusion of a temporal 1D convolutional (Conv1D) front-end, and (2) a novel ‘Early Detection’ architecture featuring specialized attention biases and a timing-aware loss function, alongside a detailed analysis of model behavior during the emergence phase. This paper is organized as follows: Section 2 describes the dataset, preprocessing procedures, and the architectures of our experimental setup alongside the baseline LSTM model, detailing the loss functions and optimization strategies employed. Section 3 presents quantitative performance metrics, hyperparameter search results, and detailed evaluation within emergence windows, supported by representative diagnostic plots. Section 4 interprets our findings, examining

the trade-offs between statistical accuracy and physical plausibility of forecasts. Finally, Section 5 summarizes our key contributions and outlines directions for future research.

2 Methodology

2.1 Dataset and Preprocessing

Our analysis utilizes SolARED (Kasapis, Dogan, et al., 2025), a machine learning-ready dataset, comprising 50 active regions observed with the SDO/HMI instrument. Each region, covering an area of $30.66^\circ \times 30.66^\circ$, was remapped onto the heliographic coordinates using the azimuthal equidistant (Postel's) projection centered its midpoint, and tracked using the Carrington rotation rate for a continuous 10-day period encompassing the phases surrounding emergence. From the original 50 regions, 4 were excluded due to data gaps and quality issues. The remaining 46 ARs were partitioned into a training/validation set of 41 regions and a held-out test set of 5 regions. While the source dataset contains 2D spatial maps (512×512 pixels), we extract 1D time series for modeling by averaging the pixel values within each tile. The acoustic power maps (P_a) in the dataset are calculated from Doppler velocity measurements (v_D). The utilized dataset also includes line-of-sight magnetic field (B_{los}), and continuum intensity (I_c) maps. Each tracked region within each emerging AR is partitioned into a 9×9 grid. Following Kasapis, Kitiashvili, et al. (2023), we primarily utilize the central row (9 tiles) of the tracked grid for model training to balance the distribution of quiet and emerging samples. However, since the model processes row-wise sequences independently, it can be applied to any row within the AR grid during inference. To correct for solar center-to-limb variations, the SolARED dataset normalizes the data relative to the top and bottom rows, effectively enhancing magnetic activity signals by subtracting systematic variations.

We applied normalization to the input dataset to ensure consistent scaling across different emergence events as

$$X' = \frac{X - X_{min}}{X_{max} - X_{min}}, \quad (1)$$

where X represents the data (acoustic power bands and magnetic field), while X_{min} and X_{max} are global extremes computed over all tiles and observation periods. This normalization to $[0, 1]$ ensures equitable feature contribution. Time-series sequences use a sliding window with input length $L_{in} = 110$ hours and prediction horizon $L_{out} = 12$ hours. For full details on geometric correction and tiling, see Kasapis, Dogan, et al. (2025).

2.2 Transformer Architectures and Training

To isolate the specific contributions of our architectural proposals, we employ a factorial experimental design (Fisher, 1935). This approach evaluates the interaction between two independent binary factors: (1) the inclusion of a convolutional front-end (Conv1D: True/False), and (2) the attention mechanism type (Standard vs. Early Detection). This yields four distinct model configurations, allowing us to determine if these components offer additive gains or act as functional replacements.

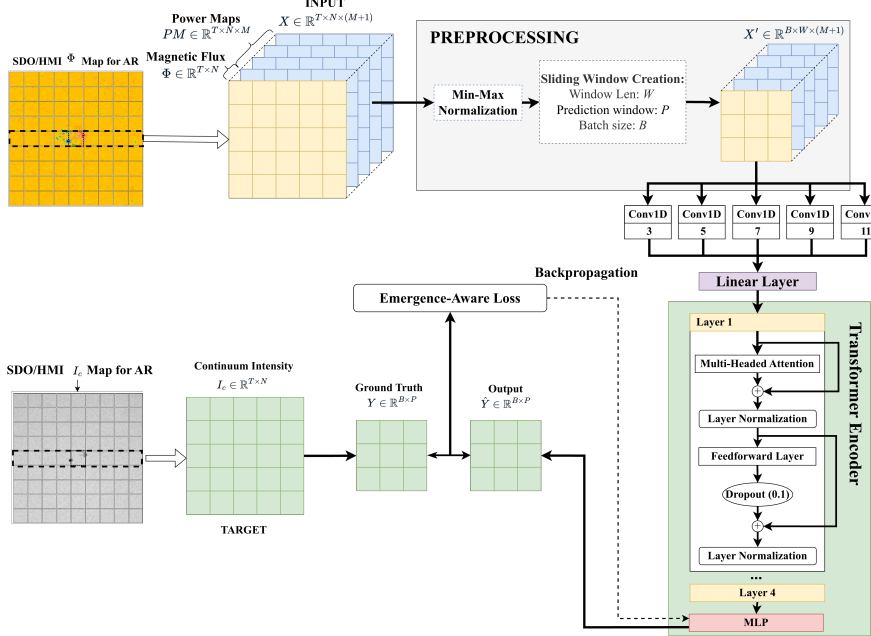


Figure 1: Schematic overview of the end-to-end machine learning pipeline for continuum intensity decrease detection during the emergence of ARs. The system extracts central tiles from the tracked SDO/HMI magnetic flux (Φ) map cut-outs, combining them with acoustic power maps to form feature tensor X . Sliding windows of length $W = 110$ are extracted with $P = 12$ prediction targets. An encoder-based Transformer predicts continuum intensity evolution \hat{Y} . Training utilizes an emergence-aware loss function optimizing MSE, early detection rewarding, and derivative loss.

We investigate a sliding-window Transformer and conduct a systematic ablation study to evaluate two key factors: the inclusion of a temporal 1D Convolutional (Conv1D) front-end, and the use of a specialized ‘Early Detection’ architecture. The complete end-to-end data processing and forecasting pipeline is illustrated in Figure 1. This results in four distinct model configurations. Figure 2 provides a visual summary of this experimental setup. The input to all model configurations consists of normalized time-series features $\mathbf{X} \in \mathbb{R}^{B \times L \times d_{in}}$, where B denotes batch size, $L = 110$ hours represents the input sequence length, and $d_{in} = 5$ corresponds to four acoustic power maps at four frequency bands (2–3, 3–4, 4–5, and 5–6 mHz), and line-of-sight magnetograms. These features capture both the subsurface acoustic signatures preceding emergence and the evolving surface magnetic field configuration.

The baseline architecture (**Baseline** and **Baseline+Conv1D**) applies standard Transformer encoder layers to fixed-length temporal segments. The model processes input sequences $\mathbf{X} \in \mathbb{R}^{L_{in} \times d_{in}}$, where $d_{in} = 5$ denotes the number of input channels per time step. Input embedding is performed via linear projection:

$$\mathbf{H}^{(0)} = \mathbf{X}\mathbf{W}_{emb} + \mathbf{P}, \quad (2)$$

where $\mathbf{W}_{emb} \in \mathbb{R}^{d_{in} \times d_{model}}$ is the embedding matrix, and $\mathbf{P} \in \mathbb{R}^{L_{in} \times d_{model}}$ is a learnable positional embedding. The Transformer encoder applies L layers of multi-head self-

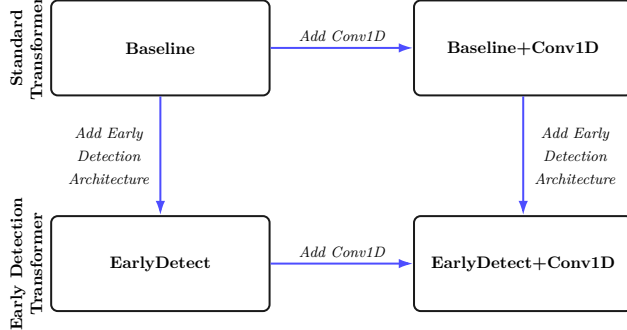


Figure 2: The factorial ablation study design. We compare two main architectures (Standard Transformer vs. Early Detection Transformer) and orthogonally evaluate the impact of a temporal 1D convolutional (Conv1D) front-end, resulting in four distinct model configurations: **Baseline**, **Baseline+Conv1D**, **EarlyDetect**, and **EarlyDetect+Conv1D**.

attention followed by feed-forward processing:

$$\mathbf{A}^{(l)} = \text{MultiHead}(\mathbf{H}^{(l-1)}), \quad (3)$$

$$\mathbf{H}^{(l)} = \text{LayerNorm}(\mathbf{H}^{(l-1)} + \mathbf{A}^{(l)}), \quad (4)$$

$$\mathbf{F}^{(l)} = \text{FFN}(\mathbf{H}^{(l)}), \quad (5)$$

$$\mathbf{H}^{(l)} = \text{LayerNorm}(\mathbf{H}^{(l)} + \mathbf{F}^{(l)}), \quad (6)$$

where $\mathbf{H}^{(l)}$ denotes the output representation of the l -th encoder layer. $\text{MultiHead}(\cdot)$ represents the multi-head self-attention mechanism, which computes temporal dependencies across the sequence. $\text{FFN}(\cdot)$ is the position-wise feed-forward network consisting of two linear transformations with a non-linear activation, and $\text{LayerNorm}(\cdot)$ denotes layer normalization. The terms $\mathbf{A}^{(l)}$ and $\mathbf{F}^{(l)}$ represent the intermediate outputs of the attention and feed-forward sub-layers, respectively.

The `MultiHead` attention includes a learnable relative positional bias, as described by Shaw et al. (2018). Finally, instead of standard global pooling, this model uses a weighted pooling mechanism. An auxiliary `emergence_detector` head assigns a salience score to each time step, and the final sequence representation \mathbf{h}_{pooled} is computed as the weighted sum of all time steps. This pooled vector is passed to a final `prediction_head` to generate the 12-hour ahead forecast $\hat{\mathbf{y}}$. The baseline models (**Baseline** and **Baseline+Conv1D**) are trained with an `emergence_aware_loss` designed to optimize for accuracy and temporal smoothness:

$$\mathcal{L}_{\text{Baseline}} = \mathcal{L}_{\text{MSE}} + \lambda_1 \mathcal{L}_{\text{deriv}} + \lambda_2 \mathcal{L}_{\text{temporal}}, \quad (7)$$

where

$$\mathcal{L}_{\text{MSE}} = \frac{1}{N} \sum_{i=1}^N (\hat{y}_i - y_i)^2 \quad (8)$$

$$\mathcal{L}_{\text{deriv}} = \frac{1}{N-1} \sum_{i=1}^{N-1} ((\hat{y}_{i+1} - \hat{y}_i) - (y_{i+1} - y_i))^2 \quad (9)$$

$$\mathcal{L}_{\text{temporal}} = \frac{1}{N-2} \sum_{i=1}^{N-2} |(\hat{y}_{i+2} - \hat{y}_{i+1}) - (\hat{y}_{i+1} - \hat{y}_i)| \quad (10)$$

Here, $\mathcal{L}_{\text{deriv}}$ penalizes inaccurate derivatives, while $\mathcal{L}_{\text{temporal}}$ encourages smooth predictions. Next, the Early Detection model (**EarlyDetect** and **EarlyDetect+Conv1D**) is a

specialized architecture designed to explicitly favor earlier predictions. It enhances the baseline in two key ways:

(1) **Enhanced Attention with Exponential Bias:** The `MultiHeadTemporalAttention` mechanism is modified to prioritize early temporal signals. We add a static exponential decay bias directly to the attention scores to systematically focus the model on the beginning of the sequence:

$$A_{i,j} = \frac{Q_i K_j^T}{\sqrt{d_k}} + \text{Bias}_j \quad (11)$$

where $\text{Bias}_j = w_{\text{early}} \cdot \exp\left(\frac{-j}{L \cdot 0.3}\right)$. Here, j represents the time step index, L is the sequence length, and w_{early} is a learnable weight. The scaling factor 0.3 controls the decay rate, effectively concentrating the attention bias within the first 30% of the temporal window. This forces the mechanism to retain high sensitivity to earlier time steps where precursor signals reside.

(2) **Focused Pooling:** The standard weighted pooling is replaced with an early-focused pooling mechanism function. This function combines the auxiliary emergence scores with a fixed, non-learnable exponential decay weight, more aggressively weighting the start of the sequence when generating the pooled representation $\mathbf{h}_{\text{pooled}}$.

The Early Detection models are trained with a composite objective function ($\mathcal{L}_{\text{Early}}$) that adds timing-specific penalties to the MSE baseline. The weights λ_{timing} and λ_{early} are hyperparameters optimized via grid search (evaluating $\lambda_{\text{timing}} \in \{0.2, 0.3, 0.4\}$ and $\lambda_{\text{early}} \in \{0.1, 0.2, 0.3\}$):

$$\mathcal{L}_{\text{Early}} = \mathcal{L}_{\text{MSE}} + \lambda_{\text{timing}} \mathcal{L}_{\text{timing_penalty}} + \lambda_{\text{early}} \mathcal{L}_{\text{early_signal}} \quad (12)$$

where the specific components are defined as:

$$\mathcal{L}_{\text{timing_penalty}} = \text{mean}(\text{ReLU}(\hat{\mathbf{y}} - \mathbf{y})) \quad (13)$$

$$\mathcal{L}_{\text{early_signal}} = \text{mean}(\text{ReLU}(\nabla \mathbf{y} - \nabla \hat{\mathbf{y}})) \quad (14)$$

The *timing penalty* applies an asymmetric cost that strictly penalizes “late” predictions (where $\hat{y} > y$ during an intensity dip) while ignoring early predictions. This forces the optimization landscape to favor premature dips over delayed reactions. The *early signal* term regularizes the derivative space, penalizing instances where the predicted gradient is shallower than the observed emergence gradient. Orthogonal to this core architecture, we evaluate a `TemporalConv1DBlocks` front-end to test the hypothesis that multi-scale 1D convolutions (kernels 3, 7, 15, 31) can extract short-term oscillatory precursors prior to global processing. Consequently, we compare models where this layer is enabled (`Baseline+Conv1D`, `EarlyDetect+Conv1D`) against those where the raw sequence is fed directly to the embedding layer (`Baseline`, `EarlyDetect`). These four model variants are summarized in Table 1.

Table 1: The Factorial Experimental Setup.

Model Configuration	Core Architecture	Loss Function	Conv1D Enabled
Baseline	Baseline	Baseline	False
Baseline+Conv1D	Baseline	Baseline	True
EarlyDetect	Early Detection	Early Detection	False
EarlyDetect+Conv1D	Early Detection	Early Detection	True

We employ two training methodologies: Baseline and Early Detection. A critical distinction from the LSTM baseline (Kasapis, Kitiashvili, et al., 2023), which utilizes independent optimization per tile sequence, is our use of global parameter optimization.

Our Transformer learns a single set of global weights across all active regions and tiles without shuffling. This constraint forces the model to learn spatially invariant representations, ensuring that attention patterns represent fundamental emergence signatures rather than tile-specific idiosyncrasies. The unified training framework is outlined in Algorithm 1.

Algorithm 1 Unified Training Algorithm for Factorial Transformer Ablation Study

```

1: Input: Training dataset  $\mathcal{D}_{train}$ , Model Configuration  $M_{config}$ 
2: Initialize AdamW optimizer, OneCycleLR scheduler
3:
4: for each epoch do
5:   for each batch  $(X, Y)$  in  $\mathcal{D}_{train}$  do
6:     Move batch to GPU
7:     if  $M_{config} \in \{\text{Baseline+Conv1D}, \text{EarlyDetect+Conv1D}\}$  then            $\triangleright$  Apply Conv1D
8:        $X \leftarrow \text{TemporalConv1DBlocks}(X)$ 
9:     end if
10:
11:    if  $M_{config} \in \{\text{Baseline}, \text{Baseline+Conv1D}\}$  then            $\triangleright$  Compute for Baseline arch
12:       $\hat{Y} \leftarrow \text{BaselineModel}(X)$ 
13:       $\mathcal{L} \leftarrow \mathcal{L}_{Baseline}(\hat{Y}, Y)$             $\triangleright$  Use loss from Eq. 7
14:    else if  $M_{config} \in \{\text{EarlyDetect}, \text{EarlyDetect+Conv1D}\}$  then
15:       $\hat{Y} \leftarrow \text{EarlyDetectionModel}(X)$ 
16:       $\mathcal{L} \leftarrow \mathcal{L}_{Early}(\hat{Y}, Y)$             $\triangleright$  Use loss from Eq. 12
17:    end if
18:    Zero gradients, backward, step optimizer, clip gradients, scheduler step
19:  end for
20:  Perform validation and checkpoint the best model
21: end for

```

The unified training framework is outlined in Algorithm 1. The conditional logic (lines 7-17) explicitly implements the four branches of our ablation study. The model first selects whether to apply the `TemporalConv1DBlocks` preprocessing (lines 7-9). It then passes the features to either the `Baseline` or `EarlyDetect` architecture and computes the loss using the corresponding objective function ($\mathcal{L}_{Baseline}$ or \mathcal{L}_{Early}), as defined in Eqs. 7 and 12.

3 Results and Analysis

3.1 Implementation and Evaluation Protocol

All experiments were conducted using PyTorch 2.1.0 with CUDA 12.1 on NVIDIA A100 GPUs (40 GB memory) hosted on the NJIT High Performance Computing (HPC) facility. Training utilized mixed-precision arithmetic (FP16) via PyTorch’s Automatic Mixed Precision (AMP) to accelerate computation while maintaining numerical stability. We used a batch size of 32 and the AdamW optimizer with OneCycleLR scheduling. The maximum learning rates were optimized individually for each model configuration (ranging from 5×10^{-5} to 1×10^{-3} ; see Appendix A for exact values), and gradient clipping with a maximum norm of 1.0 to stabilize training. Early stopping was applied based on validation loss with a patience of 50 epochs. We conducted a separate hyperparameter search for each of the four experimental configurations to find the optimal settings for each. The search space included embedding dimension (d_{model}), number of attention heads, number of encoder layers, dropout rate, and learning rate. For the Early Detection models, we also tuned the loss component weights, such as λ_{early}

and λ_{timing} . The final configurations used for our analysis represent the best-performing model from each of these distinct searches.

The optimal architectural parameters resulting from this search are summarized in Table 2. The complete hyperparameter search spaces and final detailed configurations for all models are provided in Appendix A (Tables A1 through A5).

Table 2: Optimal architectural hyperparameters identified via grid search.

Model	Core Type	Conv1D	Encoder Layers	Attn. Heads	d_{model}
LSTM	RNN	No	3	N/A	64 (Hidden)
Baseline	Transformer	No	3	4	128
Baseline+Conv1D	Transformer	Yes	5	4	256
EarlyDetect	Transformer	No	6	8	256
EarlyDetect+Conv1D	Transformer	Yes	4	4	512

Model performance was assessed on the held-out test ARs using a comprehensive, multi-model evaluation pipeline. This approach is designed to accurately separate the model’s predictive timing from its physical accuracy by overlaying all models on the same plots.

- (1) **Emergence Timing Error (ΔT):** We calculate the temporal derivative of the normalized signal, y_t . The emergence onset time t_{onset} is defined as the *first* time step of a window where the smoothed derivative falls below a threshold $\delta = -0.01$ for a sustained duration of $k = 4$ consecutive hours. This criterion is strictly enforced across all test regions to ensure robustness against false positives induced by transient solar noise. We note that this $k = 4$ duration is more conservative than the $k > 3$ hours threshold used by Kasapis, Kitiashvili, et al. (2023), ensuring that our reported advance-warning times represent sustained physical emergence. The timing error is calculated as $\Delta T = t_{onset}^{pred} - t_{onset}^{true}$. Consequently, a negative value for ΔT indicates an early (advance) prediction, while a positive value indicates a late forecast.
- (2) **Emergence RMSE ($RMSE_{emerg}$):** Unlike overall RMSE, which is dominated by the quiet Sun baseline, this metric focuses exclusively on the dynamic emergence phase. We define the emergence window as a fixed 24-hour period starting from the detected onset: $[t_{onset}^{true}, t_{onset}^{true} + 24h]$.

$$RMSE_{emerg} = \sqrt{\frac{1}{24} \sum_{t=0}^{23} (y_{t_{onset}+t}^{denorm} - \hat{y}_{t_{onset}+t}^{denorm})^2} \quad (15)$$

This metric is computed on denormalized (physical) values to ensure operational relevance.

To ensure our metrics rigorously assess the model’s ability to capture physical emergence rather than quiet-Sun background noise, we applied specific selection criteria to the test set evaluation. While the training set utilized the geometric center (Row 4), for the test Active Regions we selected the specific row intersecting the primary flux emergence site (varying between Rows 3, 4, and 5) to target the strongest physical signal. Furthermore, although the model outputs predictions for the full 9-tile width, we limit our quantitative reporting and visualization to the central 7 tiles (indices 1–7), excluding the quiescent leftmost and rightmost edges.

To facilitate a nuanced analysis of these targeted areas, we generated a comprehensive *multi-tile diagnostic plot* for each test AR. Figure 3 shows the forecast delivered

by all considered models (LSTM and all four Transformer configurations) across the seven central tiles of active region AR13183. Each tile features a five-panel display:

- **Intensity Forecast:** The main plot showing the denormalized, physical continuum intensity for the observed data and all five model predictions.
- **Observed Derivative:** The temporal derivative of the observed intensity, used for timing.
- **LSTM Derivative:** The temporal derivative of the LSTM prediction.
- **EarlyDetect Derivative:** The temporal derivative of the best-performing Transformer.
- **Absolute Error:** The absolute error of all five models over time.

This unified visualization allows for a direct, tile-by-tile qualitative comparison of model behavior, while the aggregated metrics (mean and standard deviation across all selected tiles for an AR) are exported to a separate table for quantitative analysis.

3.2 Results

We evaluated the best-performing model from each of the four experiments and the LSTM baseline on the held-out test dataset. Performance was measured using the metrics defined in our evaluation protocol (Section 3.1), including overall RMSE, emergence RMSE (RMSE computed only within the emergence window), and the emergence Timing Difference. The results in Table 3 allow for a clear analysis of the two factors we tested. The optimal hyperparameters for the best-performing **EarlyDetect** model were identified as $\lambda_{\text{timing}} = 0.4$ and $\lambda_{\text{early}} = 0.3$, alongside a model architecture of 6 encoder layers, 8 attention heads, and an embedding dimension of 256. These optimized loss weights indicate that a stronger penalty on late predictions was necessary to force the temporal shift. The Early Detection architecture proved to be the most critical factor for success. This is best demonstrated by comparing the models without the Conv1D layer (**Baseline** vs. **EarlyDetect**). Upgrading from the **Baseline** to the **EarlyDetect** model yielded the most significant performance gain. It improved the Transformer’s Overall RMSE ($0.1239 \rightarrow 0.1189$), improved the Emergence RMSE ($0.1586 \rightarrow 0.1450$), and critically, flipped the emergence timing from 8.27 hours *late* to 4.73 hours *early*—a total improvement of 13 hours, all while maintaining a similar parameter count (5.0M vs 5.8M). In contrast, when the Conv1D layer was present (**Baseline+Conv1D** vs. **EarlyDetect+Conv1D**), upgrading the architecture had an unclear impact: RMSEs were comparable ($0.1303 \rightarrow 0.1299$), timing slightly worsened ($+6.92\text{h} \rightarrow +7.20\text{h}$), and the parameter count increased substantially ($5.6\text{M} \rightarrow 19.1\text{M}$).

Table 3: Summary of the factorial ablation study. Bold values indicate the best performance for each metric. The **EarlyDetect** model (No Conv1D) achieved the best overall performance, including the lowest RMSE and the only negative (early) timing difference (in hours).

Metric	LSTM	Baseline	Baseline+Conv1D	EarlyDetect	EarlyDetect+Conv1D
Overall RMSE	0.1330	0.1239	0.1303	0.1189	0.1299
Timing Difference	$+0.14\text{h}$	$+8.27\text{h}$	$+6.92\text{h}$	-4.73h	$+7.20\text{h}$
Emergence RMSE	0.1732	0.1586	0.1464	0.1450	0.1571
Model Parameters	184.6K	5.0M	5.6M	5.8M	19.1M

Conversely, the temporal Conv1D front-end was found to be detrimental. When added to the Baseline model (**Baseline** vs. **Baseline+Conv1D**), it worsened the Over-

all RMSE ($0.1239 \rightarrow 0.1303$), though it modestly improved the emergence RMSE ($0.1586 \rightarrow 0.1464$). The effect was similarly detrimental on the Early Detection model (**EarlyDetect** vs. **EarlyDetect+Conv1D**). Adding the Conv1D layer (**EarlyDetect+Conv1D**) hurt both the Transformer’s overall RMSE ($0.1189 \rightarrow 0.1299$) and emergence RMSE ($0.1450 \rightarrow 0.1571$) and dramatically increased the model size ($5.8\text{M} \rightarrow 19.1\text{M}$). In both cases, the Conv1D front-end added computational complexity and parameters while failing to improve—and in most cases, actively harming—model performance. Our study reveals a clear and decisive outcome. The specialized architectural biases and timing-aware loss function of the Early Detection models proved to be the most critical factors for generating operationally viable early predictions. A detailed comparison of the four experiments clarifies these findings:

- *Baseline Models (Baseline & Baseline+Conv1D)*: These models served as a crucial control. While their overall RMSEs were respectable (0.1239 and 0.1303 , respectively), their inability to predict the emergence in advance ($+8.27\text{h}$ and $+6.92\text{h}$ timing) highlights the limitations of a standard Transformer architecture, even when trained with a derivative-aware loss.
- *Early Detection + Conv1D (EarlyDetect+Conv1D)*: This configuration had the highest parameter count by a wide margin (19.1M) while showing degraded RMSE (0.1299) and the second-worst timing ($+7.20\text{h}$).
- *Early Detection - Conv1D (EarlyDetect)*: This model yielded the strongest aggregate performance. By utilizing the specialized Early Detection architecture without the Conv1D layer, it achieved the best performance in every key metric: the lowest Overall RMSE (0.1189), the lowest Emergence RMSE (0.1450), and a highly efficient parameter count (5.8M). Most importantly, it was the *only* configuration to achieve an advanced forecast, predicting the emergence 4.73 hours early.

To validate that the timing improvements were not driven by outliers or local tile variances, we analyzed the distribution of forecasting errors across the five test active regions (ARs 11698, 11726, 13165, 13179, 13183). For each AR, we calculated the mean timing difference between the predicted and observed onset of emergence (ΔT) across the seven central tiles to generate a single representative metric per region. Table 4 details the statistics of these AR-level aggregates ($N = 5$), highlighting the median timing shift and the percentage of regions successfully forecasted in advance.

Table 4: Prediction forecasting patterns. This table details the distribution of timing errors across the five test ARs. Bold values indicate the best performance for each metric. The best-performing model configuration (**EarlyDetect**) and its superior metrics (earliest mean/median timing and highest percentage of early forecasts) are shown in bold.

Model	Mean ΔT (hrs)	Median ΔT (hrs)	Std. Dev. (hrs)	% Early ($< 0\text{h}$)	% Late ($> 0\text{h}$)
LSTM	0.36	0.67	14.76	40.0	60.0
Baseline	3.71	8.75	12.94	40.0	60.0
Baseline+Conv1D	6.92	11.00	11.98	40.0	60.0
EarlyDetect	-4.73	-9.40	14.64	60.0	40.0
EarlyDetect+Conv1D	7.20	8.00	13.26	40.0	60.0

The data in Table 4 reinforce the improved global detection capability of the EarlyDetect architecture, though it also highlights a trade-off between stability and sensitivity. While the baseline models and the Conv1D variants skew towards late predictions (median offsets ranging from $+8.00\text{h}$ to $+11.00\text{h}$), the **EarlyDetect** model achieves a median timing difference of -9.40 hours. Furthermore, it is the only configuration that

achieves a majority of early forecasts (60%), compared to the 40% rate observed in all other models. The standard deviation (14.64 hours) and high variance in per-AR metrics (e.g., AR 11726 RMSE ± 956) reflect this sensitivity trade-off: the model’s noise is a direct consequence of its ability to react to micro-changes in precursor signals. This volatility is operationally preferable to the false stability of over-smoothed models that miss early onset entirely. The **EarlyDetect** model systematically shifts the predictive distribution toward earlier detection, with the magnitude of lead time varying based on the strength and clarity of precursor signatures in each active region. Detailed performance metrics for the five test active regions is presented in Appendix B (Tables B1–B5).

We also evaluated the performance of the models for each testing active region. For instance, Table 5 provides the mean metrics and standard deviations for AR13183, averaged across the seven central tiles. These metrics are computed on the denormalized, physical data. Specifically, we reverse the min-max scaling (from the [0, 1] range) to restore physical intensity units to enable comparison with observations.

Table 5: Mean qualitative metrics for AR13183. Metrics are averaged across the central tiles 38-44. Bold values indicate the best performance for each metric.

Metric		LSTM	Baseline	Baseline +Conv1D	EarlyDetect	EarlyDetect +Conv1D
Overall RMSE	Mean	416.41	328.78	410.38	328.27	389.59
	(Std)	(268.03)	(165.90)	(222.10)	(143.74)	(175.88)
Timing difference (h)		+7.50	+8.75	+11.33	+4.75	+8.00
Emergence RMSE	Mean	516.80	667.83	807.40	516.93	706.81
	(Std)	(276.63)	(44.04)	(252.02)	(146.41)	(209.34)
Model parameters		184.6K	5.0M	5.6M	5.8M	19.1M

For this specific test AR, the **EarlyDetect** model (5.8M parameters) was most operationally useful, achieving the best predictive timing (+4.75 hours) and the lowest Overall RMSE (328.27). This case highlights the difference between statistical fit (Overall RMSE) and the capture of event dynamics (Timing/Emergence RMSE). The **Baseline** model, for example, had a similar Overall RMSE (328.78) but far worse timing (+8.75 hours) and Emergence RMSE (667.83). Visual inspection of the emergence profile from Figure 3 reveals that AR 13183 exhibits a notably smoother continuum intensity drop-off and a more gradual return to the mean compared to the sharper, more volatile transitions observed in other test regions (e.g., AR 11698). Despite this naturally smooth morphology, the Conv1D layer’s smoothing effect remains detrimental: **EarlyDetect+Conv1D** (19.1M parameters) achieved worse timing (+8.00h), higher Overall RMSE (389.59), and higher Emergence RMSE (706.81) compared to **EarlyDetect**. This demonstrates that even for events with inherently smooth profiles, the Conv1D layer’s temporal filtering degrades performance by averaging out critical precursor signals that the Early Detection attention mechanism is designed to capture.

While previous metrics represent spatial averages across central tiles, Table 6 details tile-level alarm timing. This breakdown clarifies the divergence between LSTM stability and Transformer sensitivity. The LSTM tends to issue synchronous alarms, yielding low variance but late predictions. In contrast, EarlyDetect exhibits significant per-tile variance, driven by its sensitivity to local precursors. For instance, in AR11698, it triggers alarms as early as -70 hours on specific tiles, while the LSTM remains reactive. This volatility is inherent to high-sensitivity detection: the model prioritizes early warn-

ing over uniformity, accepting localized false positives for the critical benefit of earlier detection—an essential trade-off for operational forecasting.

Table 6: Comparison of emergence alarms (in hours) for the best-performing Transformer(**EarlyDetect**) vs. the LSTM Baseline. Note: Negative values indicate early (advance) detection; positive values indicate late detection. "Quiet" indicates correct rejection. FP = False Positive; FN = False Negative.

AR (Tiles)	Model	T1	T2	T3	T4	T5	T6	T7
11698 (47–53)	LSTM	Quiet	FN	8h	61h	12h	11h	Quiet
	EarlyDetect	Quiet	FN	-41h	61h	-70h	11h	FP
11726 (38–44)	LSTM	Quiet	Quiet	14h	-27h	3h	-27h	-6h
	EarlyDetect	Quiet	Quiet	18h	-31h	0h	-27h	-7h
13165 (29–35)	LSTM	Quiet	Quiet	-33h	-12h	5h	-43h	Quiet
	EarlyDetect	Quiet	Quiet	-67h	2h	6h	-46h	FP
13179 (38–44)	LSTM	Quiet	Quiet	-8h	0h	10h	FP	Quiet
	EarlyDetect	Quiet	Quiet	21h	16h	14h	Quiet	Quiet
13183 (38–44)	LSTM	Quiet	Quiet	14h	7h	8h	1h	Quiet
	EarlyDetect	Quiet	Quiet	9h	5h	4h	1h	FP

Having established this context, we present a comprehensive diagnostic plot in Figure 3 to visually confirm these findings. This unified visualization overlays five models across the seven central tiles, allowing for a direct, tile-by-tile qualitative comparison. The figure corroborates the metrics in Table 5: the **EarlyDetect** (red) prediction aligns best with the observed drops, while the **Baseline+Conv1D** is visibly late. Supplementary plots for the remaining test ARs following this same format are provided in Appendix C (Figures C1–C4).

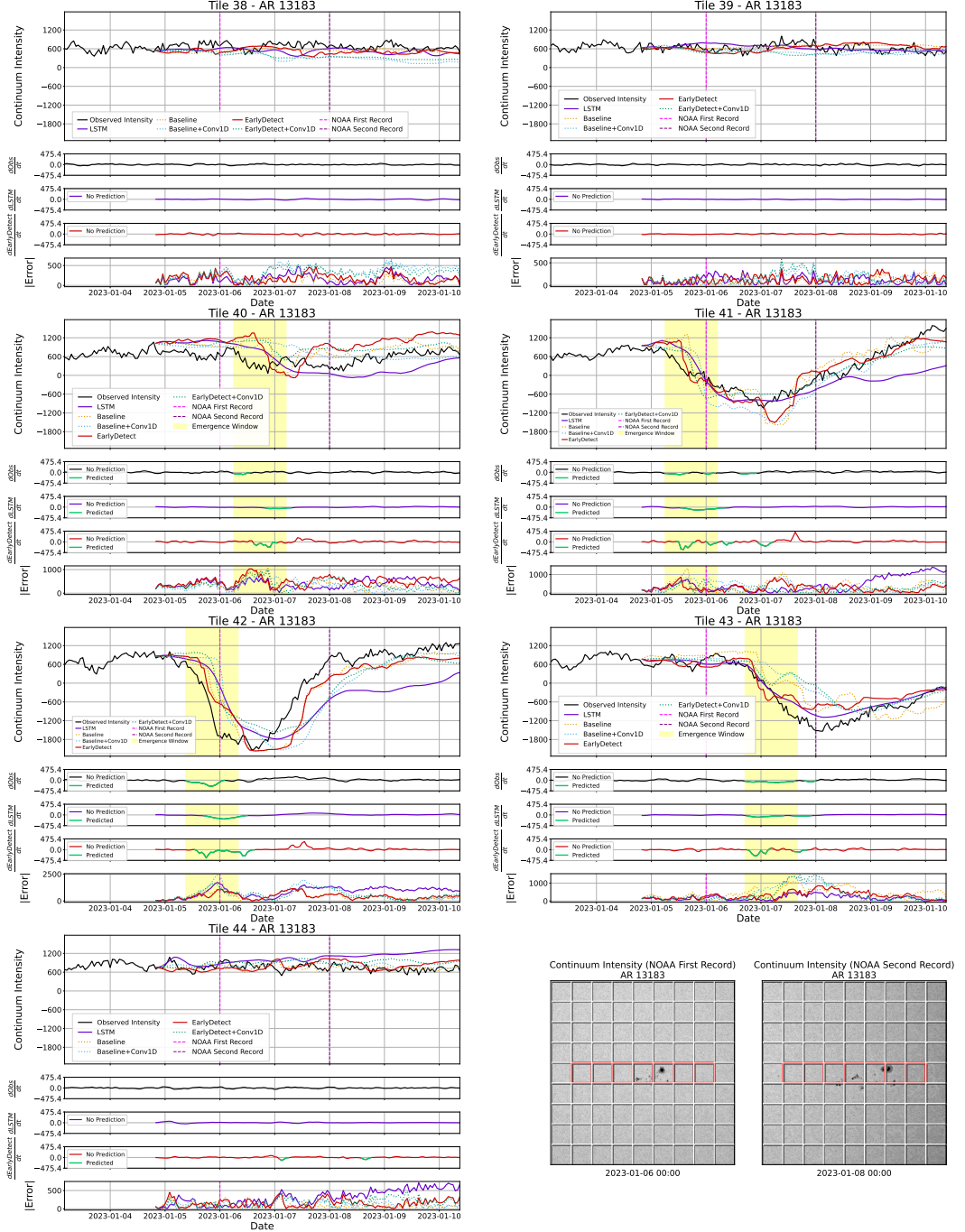


Figure 3: Comparison of predicted and actual evolution of the continuum intensity of AR13183 for seven central tiles (indicated in the right bottom corner). Each tile includes five subplots: (1) Main intensity forecast with all models overlaid, (2) Observed derivative, (3) LSTM derivative, (4) EarlyDetect derivative, and (5) Absolute error for all models. The lower-right corner includes two 9x9 continuum maps showing the AR at the start and end of the plotted window. The presented results are denormalized to physical units and reflect variations relative to the quiet Sun, which is considered as background.

To evaluate the practical trade-offs of our four Transformers models, we profiled their computational and memory costs. We compared them against the baseline LSTM and measured: (1) Computational Complexity in floating-point operations (FLOPs), (2) peak GPU memory usage during a forward pass, and (3) inference latency (Forward Pass Time). The results are detailed in Table 7.

Table 7: Model complexity and efficiency metrics.

Model	# Parameters	FLOPs	Peak Memory	Fwd. Pass Time
		(G)	(MB)	(ms)
LSTM	184.6K	0.69	55.5	2.79
Baseline	5.0M	40.4	483.5	5.50
Baseline+Conv1D	5.6M	44.8	538.6	6.40
EarlyDetect	5.8M	46.8	661.4	7.14
EarlyDetect+Conv1D	19.1M	153.1	1042.0	11.81

The analysis reveals several key findings:

- **Overall Cost:** All Transformer models are significantly more expensive than the LSTM baseline, requiring 8-18 times more memory and 60-220 times more FLOPs.
- **Impact of Conv1D:** The Conv1D layer consistently adds overhead. Comparing the Baseline model to **Baseline+Conv1D**, the Conv1D layer adds 0.6M parameters, 4.4G FLOPs, 55MB of memory, and 1ms of latency.
- **Cost of Early Detection:** The Early Detection architecture (**EarlyDetect**) is slightly more costly than the simple **Baseline**, adding 0.8M parameters and 1.6ms of latency, but is comparable in efficiency.
- **The Worst Case (**EarlyDetect+Conv1D**):** The combination of the Early Detection architecture and the Conv1D layer results in a catastrophic increase in complexity. This model is 3.3 times larger than our best model (**EarlyDetect**), requires 3.3 times the FLOPs, and is the slowest to run.

This analysis strongly reinforces our earlier findings. The optimal model, **EarlyDetect**, provides superior accuracy and timing (a -4.73h forecast) for only a minor computational cost compared to the **Baseline**. Conversely, **EarlyDetect+Conv1D** is the worst-performing model, as it is both highly inaccurate (a +7.20h lag) and by far the most computationally expensive.

4 Discussion

The comparative ablation study yielded a clear trade-off between smoothness and sensitivity. While the LSTM baseline and Baseline Transformer models produce smoother, visually appealing forecasts, they consistently lag behind the actual emergence, rendering them operationally inadequate for advance warning. The specialized Early Detection Transformer (**EarlyDetect**) was the only model to achieve the primary operational objective: a true forecast with an average lead time of -4.73 hours. The analysis of the four experiments reveals a critical decoupling of statistical accuracy (RMSE) from predictive timing (ΔT). The baseline Transformer models (**Baseline** & **Baseline+Conv1D**) achieved respectable RMSE scores but produced forecasts that were operationally useless, lagging the actual emergence by +6.92 to +8.27 hours. Similarly, the baseline LSTM, while computationally efficient, achieved only synchronous detection (+0.14h) and failed to provide a true advance warning. This demonstrates that a standard model, when op-

timized with a generic or even a derivative-aware loss function ($\mathcal{L}_{Baseline}$), will learn to produce a statistically accurate “best fit” of the emergence event, which it achieves by placing the predicted dip after the event has already begun. The success of **EarlyDetect**, therefore, is almost entirely attributable to the specialized `early_detection_loss` (\mathcal{L}_{Early}) and model attention biases. These components successfully forced the model to abandon a “perfect” physical fit and instead prioritize the subtle, early-onset signatures, achieving the primary goal of a pre-emergence warning. Remarkably, this shift in priority did not compromise overall accuracy; **EarlyDetect** simultaneously achieved the lowest RMSE of all models (0.1189), demonstrating that high-sensitivity forecasting can yield superior statistical performance alongside operational utility.

Our results reveal a critical distinction between smooth, conservative predictions and operationally useful early warnings. While the LSTM baseline and Baseline Transformer models produce smoother, visually appealing forecasts, they consistently lag behind the actual emergence. For instance, in AR 13165, the **Baseline** model predicted the emergence +10.5 hours late (averaged across tiles), while **EarlyDetect** achieved a mean advance warning of -26.25 hours—a difference of over 36 hours. Similarly, in AR 11698, the LSTM baseline was on average +23.0 hours late compared to **EarlyDetect**’s mean -9.75 hour early detection. This pattern holds across the aggregate metrics: while the LSTM achieves synchronous detection (global mean $+0.14$ h), the **EarlyDetect** Transformer systematically provides advance warnings (mean -4.73 h) with a 60% early detection rate versus the LSTM’s 40%. The LSTM’s per-tile optimization strategy, while producing visually stable fits, fundamentally fails to capture the subtle precursor signals that precede emergence. In contrast, the **EarlyDetect** model’s attention mechanism is specifically tuned to detect these early signatures, resulting in higher variance but operationally critical lead times. This higher variance—evident in metrics like AR 11726’s RMSE standard deviation of ± 956 —is a necessary trade-off for sensitivity: the model is “noisy” because it reacts to micro-changes in the acoustic power signatures, whereas the LSTM and Conv1D models are “over-smoothed” and miss the earliest onset signals entirely.

This difference in stability is further influenced by the training scope. The LSTM baseline benefited from a per-tile optimization strategy (fresh optimizer per sequence), allowing it to adapt closely to specific local dynamics. In contrast, our Transformer was constrained to a single global optimizer across all regions without shuffling. While this global approach likely contributed to the higher variance in specific edge cases (e.g., AR 11698) as the model could not overfit to local variations, the fact that the **EarlyDetect** model still achieved a 10.6% improvement in RMSE suggests it has learned a more fundamental, generalized representation of emergence physics.

Conversely, the temporal 1D convolutional (Conv1D) front-end was found to be decisively detrimental. Our hypothesis was that the Conv1D layer would help by extracting local, temporal features from the input sequences. The results from the **EarlyDetect+Conv1D** model prove this hypothesis wrong. In the most extreme case (AR 11698), the addition of the Conv1D layer collapsed the mean forecast from a -9.75 hour advance warning to a $+26.00$ hour delay. The Conv1D layer not only caused a substantial increase in model parameters and computational cost (from 5.8M to 19.1M) but also worsened all key metrics, including a 13-hour degradation in timing compared to **EarlyDetect** (-4.73 h \rightarrow $+7.20$ h). We interpret this as the Conv1D layer “over-smoothing” the input data, effectively averaging out the very faint precursor signals that the Early Detection attention mechanism was designed to find. The unique performance of AR 13183 supports this “over-smoothing” hypothesis by acting as the exception that proves the rule. As noted, AR 13183 is characterized by a naturally smooth drop-off and recovery profile. In this specific instance, the smoothing properties of the convolutional front-end likely aligned with the physical morphology of the event, acting as a beneficial filter against high-frequency noise. However, for the majority of active regions which are defined by rapid, sharp, and

faint emergence signatures, this same smoothing effect washes out the critical precursor signals, resulting in the degraded performance seen in the aggregate metrics.

The optimal model (**EarlyDetect**) performed best when fed the raw, unfiltered time series. This suggests that the self-attention mechanism is superior to both convolutional layers and the recurrent gates of the LSTM at isolating the specific acoustic power signatures (specifically in the 3-5 mHz range) that precede emergence, without requiring pre-filtering or manual band selection often necessary in prior works (e.g., Ilonidis et al., 2011; Leka et al., 2013). Unlike the smoothed models, **EarlyDetect** exhibits a characteristic pre-emergence dip in its predictions (e.g., AR 13165 Tile 31; AR 11698 Tiles 49 & 51), effectively “flagging” the region hours before the flux officially rises. This qualitative signal shape—a subtle but persistent downward trend preceding the main intensity drop—is the direct result of the model’s attention biases and timing-aware loss function, which force the architecture to prioritize early-onset signatures over statistical fit. This demonstrates that for this forecasting task, a specialized architecture that directly optimizes for predictive timing is superior to a generic model. Furthermore, the failure of the **EarlyDetect+Conv1D** model suggests a conflict between the two architectural components. This model had the highest parameter count (19.1M), a degraded RMSE (0.1299), and poor timing (+7.20h). We hypothesize that the features extracted by the Early Detection attention mechanism are made redundant or, worse, are actively harmed by the Conv1D layer’s smoothing, resulting in a bloated and inefficient model.

Our evaluation yields a mean timing difference of +0.14 hours for the LSTM baseline, which differs from the lead times of –10 to –29 hours reported by Kasapis, Kitiashvili, et al. (2023). This discrepancy is attributable to the standardized evaluation protocol employed in this study. While we utilized the same per-active-region input window lengths (e.g., 72 hours for AR11726, 96 hours for others) to account for limb proximity, we enforced a uniform emergence criterion ($k = 4$ hours, $\delta = -0.01$) and a fixed metric calculation across the entire test set. Unlike previous approaches that may have benefited from per-event threshold tuning, our standardized protocol prevents the exploitation of “lucky” early precursors. Under these rigorous conditions, the LSTM’s aggregate behavior converges on the emergence onset (synchronous detection), despite achieving significant lead times in isolated cases (e.g., AR 13165). In contrast, the Transformer systematically shifts the predictive distribution toward earlier detection, reinforcing the necessity of the attention mechanism to isolate faint precursor signals consistently.

It is crucial to distinguish between the experimental lead times reported here and the constraints of a real-time operational environment. Kasapis, Kitiashvili, et al. (2023) identified the operational latency inherent to this pipeline, primarily driven by the time required for Dopplergram sequence processing. However, the architecture’s 12-hour prediction horizon ($L_{out} = 12$) serves as a critical buffer against this latency. Because the model projects continuum intensity evolution 12 hours into the future, it theoretically maintains an operational visibility window of approximately 8 hours (12–4 hours processing latency), provided the emergence signature is detected within the forecast horizon. Our results indicate that the **EarlyDetect** model not only utilizes this horizon but also exhibits a raw timing bias of –4.73 hours (detecting signatures well before the strict onset criteria). This combination—a long prediction horizon canceling the processing delay, coupled with a hypersensitive early detection mechanism—suggests that the system remains operationally viable even under strict real-time constraints.

These results provide a strong foundation for future work. The successful architecture of **EarlyDetect** can now be applied to the more challenging but valuable task of forecasting the magnetic flux emergence, which is known to precede the continuum intensity decrease. Furthermore, this work was limited to 1D temporal sequences from individual tiles; a natural successor would be a spatio-temporal model that incorporates information from neighboring tiles, potentially providing more contextual data to improve the forecast further. Finally, the stark difference in performance between the base-

line models and the Early Detection model highlights a critical takeaway for the field: for space weather forecasting, where advance warning is the primary objective, low RMSE must not be mistaken for a useful forecast.

5 Conclusion

In this work, we address the need for timely and accurate forecasting of solar active region emergence. We developed and evaluated a series of Transformer-based models in a systematic ablation study, comparing a novel Early Detection architecture against a standard Transformer baseline, with and without a temporal Conv1D front-end. We measured success not only by statistical accuracy (RMSE) but by predictive timing (Δ Emergence), a metric crucial for operational space weather. We found that the standard Transformer architecture, while achieving low error, failed to produce a timely forecast, lagging the emergence by over 8 hours. The addition of a Conv1D front-end was detrimental, increasing model complexity and harming performance. Our results identify a distinct trade-off between the reactive stability of recurrent models and the proactive sensitivity of attention-based architectures. The specialized Early Detection Transformer (**EarlyDetect**), which paired a biased attention mechanism with a timing-aware loss function, was the only configuration to provide a true advance forecast, predicting the emergence 4.73 hours early. It also achieved the best statistical accuracy, with an overall RMSE of 0.1189 and an Emergence RMSE of 0.1450, representing a 10.6% improvement over the LSTM baseline. Crucially, these results were established under a stricter, uniform emergence criterion ($k = 4$ hours) compared to previous studies, ensuring that the reported advance warnings represent sustained physical emergence rather than transient noise. However, our analysis suggests that specific magnetic morphologies may present stability challenges that challenge the Transformer’s attention mechanism more than the conservative gates of the LSTM. Future work must expand the evaluation to a larger cohort of Active Regions to smooth out these potential selection biases and definitively establish the stability of the attention-based approach.

The observed performance characteristics of our Transformer-based model suggest several directions for architectural refinement. While the attention mechanism excels at capturing global temporal patterns, the quadratic computational complexity may limit scalability to longer sequences. Recent state-space models (Gu & Dao, 2024; Pandey et al., 2024) offer linear-time alternatives that maintain competitive performance while enabling efficient processing of extended temporal contexts. Moreover, models implementing hyperbolic geometry (Patil et al., 2025) leverage spaces with constant negative curvature to efficiently embed hierarchical structures, demonstrating superior performance on tasks requiring multi-scale reasoning as compared to their Euclidean counterparts. Such architectural diversity can provide a rich landscape for future AR emergence prediction systems, balancing computational efficiency, interpretability, and representational capacity.

This study demonstrates that Transformer architectures, when specifically modified to prioritize early-onset signals, are highly effective for AR emergence prediction. Our findings prove that simply applying deep learning is insufficient; a generic model will optimize for a statistical fit, not for an early warning. Critically, our ablation study reveals that removing Conv1D smoothing (pure **EarlyDetect**) is preferable for warning systems because the cost of false positives (noise) is outweighed by the benefit of significantly earlier detection. The specialized, timing-aware architecture provides a new, robust baseline for future research in heliophysics and a clear path toward building operationally viable forecasting systems that prioritize advance warning over statistical smoothness.

6 Code and Data Availability

The code, pre-trained models, and evaluation scripts used to produce the results presented in this manuscript are publicly available. The software is distributed under the MIT license and can be accessed at the GitHub repository: <https://github.com/jonastirona/ar-emergence-transformers>.

The repository includes:

- Pre-trained model checkpoints for all five evaluated configurations (LSTM baseline and four Transformer variants)
- Complete training and evaluation pipelines implemented in PyTorch
- Model complexity profiling tools
- Comprehensive documentation, including data format specifications and reproducibility instructions
- SLURM job scripts for HPC environments

The software requires Python 3.10+ and PyTorch 2.1.0 or later. Complete installation instructions and dependencies are provided in the repository's `README.md` file. The data used in this study can be obtained from the SolARED portal (<https://sun.njit.edu/sarportal/>).

Acknowledgments

This work was supported by the New Jersey Institute of Technology (NJIT) Grace Hopper AI Research Institute (GHAIRI) Seed Grant (Grant No. 179025). We thank the computing resources provided by the High Performance Computing (HPC) facility at NJIT. This work is supported by the NASA AI/ML HECC Expansion Program, and the NASA grants 23-HGIO23_2-0077, 20-HSR20_2-0037, 80NSSC19K0630, 80NSSC19K0268, 80NSSC20K1870, and 80NSSC22M0162. The authors acknowledge the use of ChatGPT, Gemini, and Cursor for assistance with language editing and coding.

Conflict of Interest

The authors declare no conflicts of interest relevant to this study.

References

Barnes, G., Birch, A., Leka, K., & Braun, D. (2014). Helioseismology of pre-emerging active regions. iii. statistical analysis. *The Astrophysical Journal*, 786(1), 19.

Birch, A., Braun, D., Leka, K., Barnes, G., & Javornik, B. (2012). Helioseismology of pre-emerging active regions. ii. average emergence properties. *The Astrophysical Journal*, 762(2), 131.

Fisher, R. A. (1935). *The design of experiments* (1st ed.). Edinburgh: Oliver and Boyd.

Gu, A., & Dao, T. (2024). Mamba: Linear-time sequence modeling with selective state spaces. In *First conference on language modeling*.

Hochreiter, S., & Schmidhuber, J. (1997). Long short-term memory. *Neural computation*, 9(8), 1735–1780.

Hoeksema, J. T., Liu, Y., Hayashi, K., Sun, X., Schou, J., Couvidat, S., . . . others (2014). The helioseismic and magnetic imager (hmi) vector magnetic field pipeline: Overview and performance. *Solar Physics*, 289(9), 3483–3530.

Horne, R., Glauert, S., Meredith, N., Boscher, D., Maget, V., Heynderickx, D., & Pitchford, D. (2013). Space weather impacts on satellites and forecasting the

earth's electron radiation belts with spacecast. *Space weather*, 11(4), 169–186.

Howard, R., Sheeley Jr, N., Koomen, M., & Michels, D. (1985). Coronal mass ejections: 1979–1981. *Journal of Geophysical Research: Space Physics*, 90(A9), 8173–8191.

Ilonidis, S., Zhao, J., & Kosovichev, A. (2011). Detection of emerging sunspot regions in the solar interior. *Science*, 333(6045), 993–996.

Kasapis, S., Dogan, E., Butler, J. D., Tirona, J., Patil, S., Kitiashvili, I. N., ... Kosovichev, A. G. (2025). Solared: Solar active region emergence dataset of 1d timeseries for machine learning aided predictions. *JGR: Machine Learning and Computation*. (in preparation)

Kasapis, S., Kitiashvili, I. N., Kosovichev, A. G., & Stefan, J. T. (2025). Prediction of intensity variations associated with emerging active regions using helioseismic power maps and machine learning. *The Astrophysical Journal Supplement Series*, 280(2), 64.

Kasapis, S., Kitiashvili, I. N., Kosovichev, A. G., Stefan, J. T., & Apte, B. (2023). Predicting the emergence of solar active regions using machine learning. *Proceedings of the International Astronomical Union*, 19(S365), 311–319.

Kasapis, S., Thompson, B. J., Rodriguez, J. V., Attie, R., Cucho-Padin, G., da Silva, D., ... Pesnell, W. D. (2023). Turning noise into data: Characterization of the van allen radiation belt using sdo spikes data. *Space Weather*, 21(3), e2022SW003310.

Keegan, K., Bonaventura, N., Guzmán, N., Karna, N., Hess-Webber, S., Kasapis, S., ... Muñoz-Jaramillo, A. (2025). Data-driven solar surface flux transport modeling with uncertainty quantification. In *The reach and limits of ai for scientific discovery workshop, neurips*.

Kosovichev, A., Duvall, T., & Scherrer, P. (2001). Time-distance inversion methods and results (invited review). *Helioseismic Diagnostics of Solar Convection and Activity*, 159–176.

Kosovichev, A. G., Basu, S., Bekki, Y., Buitrago-Casas, J. C., Chatzistergos, T., Chen, R., ... others (2025). Structure and dynamics of the sun's interior revealed by the helioseismic and magnetic imager. *Solar Physics*, 300(5), 70.

Leka, K. D., Barnes, G., Birch, A. C., Gonzalez-Hernandez, I., Dunn, T., Javornik, B., & Braun, D. C. (2013, January). Helioseismology of Pre-emerging Active Regions. I. Overview, Data, and Target Selection Criteria. *ApJ*, 762(2), 130. doi: 10.1088/0004-637X/762/2/130

Pak, S., Cuesta, M., Farooki, H., Khoo, L., Xu, Z., Davis, A., ... others (2025). Species-dependent variability in the energy spectra of intense solar energetic particle events observed by psp/isōis/epi-hi/let. *The Astrophysical Journal Supplement Series*, 281(1), 21.

Pandey, A. P., Varghese, A. J., Patil, S., & Xu, M. (2024). A comparative study on dynamic graph embedding based on mamba and transformers. *arXiv preprint arXiv:2412.11293*.

Patil, S., Zhang, Z., Huang, Y., Ma, T., & Xu, M. (2025). Hyperbolic large language models. *arXiv preprint arXiv:2509.05757*.

Pesnell, W. D., Thompson, B. J., & Chamberlin, P. (2012). *The solar dynamics observatory (sdo)*. Springer.

Scherrer, P. H., Schou, J., Bush, R., Kosovichev, A., Bogart, R., Hoeksema, J., ... others (2012). The helioseismic and magnetic imager (hmi) investigation for the solar dynamics observatory (sdo). *Solar Physics*, 275, 207–227.

Schrijver, C. J. (2009). Driving major solar flares and eruptions: A review. *Advances in Space Research*, 43(5), 739–755.

Shaw, P., Uszkoreit, J., & Vaswani, A. (2018). Self-attention with relative position representations. *arXiv preprint arXiv:1803.02155*.

Stefan, J. T., & Kosovichev, A. G. (2023). Exploring the connection between he-

lioseismic travel time anomalies and the emergence of large active regions during solar cycle 24. *The Astrophysical Journal*, 948(1), 1.

van Driel-Gesztelyi, L., & Green, L. M. (2015). Evolution of active regions. *Living Reviews in Solar Physics*, 12(1), 1.

Vaswani, A., Shazeer, N., Parmar, N., Uszkoreit, J., Jones, L., Gomez, A. N., ... Polosukhin, I. (2017). Attention is all you need. *Advances in neural information processing systems*, 30.

Whitman, K., Egeland, R., Richardson, I. G., Allison, C., Quinn, P., Barzilia, J., ... others (2023). Review of solar energetic particle prediction models. *Advances in Space Research*, 72(12), 5161–5242.

Wu, H., Xu, J., Wang, J., & Long, M. (2021). Autoformer: Decomposition transformers with auto-correlation for long-term series forecasting. *Advances in neural information processing systems*, 34, 22419–22430.

Zhou, H., Zhang, S., Peng, J., Zhang, S., Li, J., Xiong, H., & Zhang, W. (2021). Informer: Beyond efficient transformer for long sequence time-series forecasting. In *Proceedings of the aaai conference on artificial intelligence* (Vol. 35, pp. 11106–11115).

Appendix A Hyperparameter Configuration

To ensure reproducibility, we provide the complete hyperparameter search spaces and optimal configurations for all models evaluated in this study. Tables A1 through A4 present both the search ranges explored and the optimal values selected for each model.

Table A1: Hyperparameter optimization for the Baseline (LSTM) Model. The optimal configuration (128-dimension embedding, 3 encoder layers) was selected from this search space, resulting in one of the smaller models tested.

Parameter	Search Range	Optimal Value
Input Sequence Length (L_{in})	Fixed	110
Output Horizon (L_{out})	Fixed	12
Embedding Dimension (d_{model})	{128, 256}	128
Attention Heads	{4}	4
Encoder Layers	{3, 5}	3
Dropout	{0.0, 0.3}	0.0
Learning Rate	{ 1×10^{-4} , 1×10^{-3} }	1×10^{-3}
Temporal Conv1D	{False}	False

Table A2: Hyperparameter optimization for the **Baseline+Conv1D** Model. The optimal configuration required a larger embedding (256-dim) and more layers (5) than the standard baseline, indicating a more complex model was chosen during the search.

Parameter	Search Range	Optimal Value
Input Sequence Length (L_{in})	Fixed	110
Output Horizon (L_{out})	Fixed	12
Embedding Dimension (d_{model})	{128, 256}	256
Attention Heads	{4}	4
Encoder Layers	{3, 5}	5
Dropout	{0.0, 0.3}	0.0
Learning Rate	{ 1×10^{-4} , 1×10^{-3} }	1×10^{-4}
Temporal Conv1D	{True}	True

Table A3: Hyperparameter optimization for the **EarlyDetect** Model (Best Performer). This table includes the search space for the specialized loss weights. The optimal configuration favored a strong penalty on late predictions ($\lambda_{timing} = 0.4$) and a moderate derivative penalty ($\lambda_{early} = 0.3$), alongside a 6-layer, 8-head architecture.

Parameter	Search Range	Optimal Value
Input Sequence Length (L_{in})	Fixed	110
Output Horizon (L_{out})	Fixed	12
Embedding Dimension (d_{model})	{256, 512}	256
Attention Heads	{4, 8}	8
Encoder Layers	{4, 6}	6
Dropout	{0.0, 0.1}	0.0
Learning Rate	{ 5×10^{-5} , 1×10^{-4} , 2×10^{-4} }	2×10^{-4}
Temporal Conv1D	{False}	False
<i>Early Detection Parameters</i>		
λ_{timing}	{0.2, 0.3, 0.4}	0.4
λ_{early}	{0.1, 0.2, 0.3}	0.3
Timing Bias Weight	{0.1, 0.2, 0.3, 0.5}	0.1
Early Detection Weight (w_{early})	{0.1, 0.2, 0.3}	0.3
Internal Threshold (δ)	{-0.003, -0.005, -0.007}	-0.007

Table A4: Hyperparameter optimization for the **EarlyDetect+Conv1D** Model. This model, which had the highest computational cost, settled on the largest embedding dimension (512) but a smaller number of layers (4). The optimal loss weights ($\lambda_{timing} = 0.2$, $\lambda_{early} = 0.2$) were weaker than the more successful non-Conv1D variant.

Parameter	Search Range	Optimal Value
Input Sequence Length (L_{in})	Fixed	110
Output Horizon (L_{out})	Fixed	12
Embedding Dimension (d_{model})	{256, 512}	512
Attention Heads	{4, 8}	4
Encoder Layers	{4, 6}	4
Dropout	{0.0, 0.1}	0.0
Learning Rate	{ 5×10^{-5} , 1×10^{-4} , 2×10^{-4} }	5×10^{-5}
Temporal Conv1D	{True}	True
<i>Early Detection Parameters</i>		
λ_{timing}	{0.2, 0.3, 0.4}	0.2
λ_{early}	{0.1, 0.2, 0.3}	0.2
Timing Bias Weight	{0.1, 0.2, 0.3, 0.5}	0.3
Early Detection Weight (w_{early})	{0.1, 0.2, 0.3}	0.1
Internal Threshold (δ)	{-0.003, -0.005, -0.007}	-0.007

Table A5: Configuration for the LSTM Baseline Model (Kasapis, Kitiashvili, et al., 2025)
 Note, in this model, the hidden size (64) is significantly smaller compared to the Transformer embedding dimensions.

Hyperparameter	Value
Input Sequence Length (L_{in})	110
Output Horizon (L_{out})	12
Hidden Size	64
Number of Layers	3
Learning Rate	0.01
Training Epochs	1000

Appendix B Performance of models for test active regions

Tables B1 through B5 present comprehensive performance metrics for all models across five test active regions.

Table B1: Detailed metrics for AR 11698. This region illustrates the high-variance nature of the **EarlyDetect** model. While it achieves an early mean timing difference of -9.75h (compared to the LSTM's +23.00h lag), the extreme standard deviation (± 50.11 h) reflects its volatility: it detects emergence very early on specific tiles (e.g., Tile 51) but lacks the spatial consistency of the baseline models.

Model	Overall RMSE	Emergence RMSE	Emergence R^2	Timing Δ (h)
LSTM Baseline	649.48 ± 167.86	736.86 ± 284.69	-8.42 ± 11.05	$+23.00 \pm 21.99$
Baseline	712.97 ± 252.38	796.05 ± 299.52	-20.39 ± 32.29	-15.50 ± 59.50
Baseline+Conv1D	710.99 ± 248.03	895.66 ± 326.68	-13.46 ± 15.55	$+24.00 \pm 21.97$
EarlyDetect	659.36 ± 236.06	756.02 ± 298.05	-12.37 ± 19.05	-9.75 ± 50.11
EarlyDetect+Conv1D	690.66 ± 232.17	975.47 ± 344.66	-14.64 ± 18.49	$+26.00 \pm 21.39$

Table B2: Detailed metrics for AR 11726. This region represents a success case for early detection across all architectures. The **EarlyDetect** model achieves the earliest mean timing (-9.40h), slightly outperforming the LSTM (-8.60h). However, the high standard deviation in the Transformer's Emergence RMSE indicates that while it captures the timing effectively, the magnitude of the predicted drop varies significantly across tiles compared to the recurrent baseline.

Model	Overall RMSE	Emergence RMSE	Emergence R^2	Timing Δ (h)
LSTM Baseline	2291.49 ± 1763.68	2971.70 ± 2163.67	-36.24 ± 41.60	-8.60 ± 16.30
Baseline	1348.95 ± 1066.91	1330.51 ± 384.99	-1.82 ± 2.59	-6.20 ± 13.18
Baseline+Conv1D	1547.44 ± 1262.10	1165.09 ± 340.77	-0.91 ± 1.51	-7.40 ± 15.70
EarlyDetect	1357.54 ± 956.57	1459.25 ± 420.69	-3.86 ± 5.79	-9.40 ± 18.01
EarlyDetect+Conv1D	1620.11 ± 1463.07	1370.81 ± 91.56	-4.44 ± 7.82	-10.50 ± 13.16

Table B3: Performance metrics for AR 13165. This region provides the strongest evidence for the **EarlyDetect** architecture’s sensitivity. It achieved a substantial mean advance warning of -26.25 hours, drastically outperforming the Baseline (+10.5h late) and the LSTM (-20.75h). The large standard deviation in timing (± 31.18 h) reflects the model’s distinct response to precursors in specific tiles (e.g., Tile 31) versus others.

Model	Overall RMSE	Emergence RMSE	Emergence R^2	Timing Δ (h)
LSTM Baseline	658.94 ± 359.44	620.47 ± 290.33	-4.20 ± 5.78	-20.75 ± 18.61
Baseline	413.24 ± 140.97	506.84 ± 179.88	-1.39 ± 1.04	$+10.50 \pm 28.46$
Baseline+Conv1D	512.54 ± 138.48	448.83 ± 156.79	-1.10 ± 1.41	-6.00 ± 19.61
EarlyDetect	454.67 ± 153.67	623.33 ± 245.98	-2.62 ± 1.72	-26.25 ± 31.18
EarlyDetect+Conv1D	438.86 ± 190.73	404.64 ± 94.73	-0.74 ± 1.07	-4.00 ± 20.40

Table B4: Performance metrics for AR 13179. This region highlights a failure mode for the attention-based models in the presence of shallow or ambiguous signatures. All Transformer variants predicted the emergence significantly late (e.g., +17.00h for **EarlyDetect**), whereas the LSTM baseline proved more robust, achieving synchronous detection with a timing difference of +0.67h.

Model	Overall RMSE	Emergence RMSE	Emergence R^2	Timing Δ (h)
LSTM Baseline	844.94 ± 454.76	726.72 ± 193.19	-1.92 ± 1.34	$+0.67 \pm 7.36$
Baseline	825.32 ± 734.06	876.58 ± 323.44	-2.74 ± 1.51	$+21.00 \pm 4.24$
Baseline+Conv1D	850.56 ± 712.22	706.83 ± 281.18	-1.31 ± 0.74	$+13.00 \pm 2.00$
EarlyDetect	781.12 ± 818.34	994.92 ± 372.22	-3.53 ± 1.19	$+17.00 \pm 0.50$
EarlyDetect+Conv1D	781.12 ± 698.30	802.18 ± 366.18	-1.54 ± 0.62	$+17.00 \pm 2.94$

Table B5: Performance metrics for AR 13183. Characterized by a smooth intensity profile, this region was generally detected late by all models. However, **EarlyDetect** yielded the best performance of the group, achieving the closest timing (+4.75h) and the lowest Overall RMSE (328.27). The Conv1D front-end proved detrimental here, worsening timing to +8.00h and increasing error.

Model	Overall RMSE	Emergence RMSE	Emergence R^2	Timing Δ (h)
LSTM Baseline	416.41 ± 268.03	516.80 ± 276.63	-1.05 ± 1.96	$+7.50 \pm 4.61$
Baseline	328.78 ± 165.90	667.83 ± 44.04	-3.64 ± 5.01	$+8.75 \pm 3.56$
Baseline+Conv1D	410.38 ± 222.10	807.40 ± 252.02	-3.27 ± 3.24	$+11.33 \pm 1.25$
EarlyDetect	328.27 ± 143.74	516.93 ± 146.41	-2.54 ± 4.86	$+4.75 \pm 2.86$
EarlyDetect+Conv1D	389.59 ± 175.88	706.81 ± 209.34	-3.01 ± 4.18	$+8.00 \pm 4.24$

Table B6: Detailed emergence predictions by tile. Values indicate the lead time (in hours) relative to emergence onset. Negative values (e.g., -26h) indicate successful early detection (Good), while positive values indicate late detection (Bad). This granular view highlights the stability-sensitivity trade-off: while the `EarlyDetect` model secures the best global mean, it exhibits higher variance in specific regions (e.g., AR 11698) compared to the more conservative LSTM baseline.

Model	T1	T2	T3	T4	T5	T6	T7	Overall
AR 11698 (Tiles 47–53)								
Baseline+C1D	FP	FN	10h	62h	13h	11h	Quiet	24h
Baseline	Quiet	FN	-40h	63h	12h	-97h	Quiet	-15h
EarlyDetect	Quiet	FN	-41h	61h	-70h	11h	FP	-9h
EarlyDetect+C1D	FP	FN	12h	63h	15h	14h	Quiet	26h
LSTM	Quiet	FN	8h	61h	12h	11h	Quiet	23h
AR 11726 (Tiles 38–44)								
Baseline+C1D	Quiet	Quiet	12h	-27h	3h	-25h	0h	-7h
Baseline	Quiet	Quiet	1h	-25h	7h	-19h	5h	-6h
EarlyDetect	Quiet	Quiet	18h	-31h	0h	-27h	-7h	-9h
EarlyDetect+C1D	Quiet	Quiet	FN	-26h	4h	-21h	1h	-10h
LSTM	Quiet	Quiet	14h	-27h	3h	-27h	-6h	-8h
AR 13165 (Tiles 29–35)								
Baseline+C1D	Quiet	Quiet	-33h	2h	13h	FN	Quiet	-6h
Baseline	Quiet	Quiet	-31h	49h	8h	16h	Quiet	10h
EarlyDetect	Quiet	Quiet	-67h	2h	6h	-46h	FP	-26h
EarlyDetect+C1D	Quiet	Quiet	-32h	16h	4h	FN	Quiet	-4h
LSTM	Quiet	Quiet	-33h	-12h	5h	-43h	Quiet	-20h
AR 13179 (Tiles 38–44)								
Baseline+C1D	Quiet	Quiet	FN	15h	11h	Quiet	Quiet	13h
Baseline	Quiet	Quiet	27h	18h	18h	FP	Quiet	21h
EarlyDetect	Quiet	Quiet	21h	16h	14h	Quiet	Quiet	17h
EarlyDetect+C1D	Quiet	Quiet	FN	17h	16h	Quiet	Quiet	16h
LSTM	Quiet	Quiet	-8h	0h	10h	FP	Quiet	0h
AR 13183 (Tiles 38–44)								
Baseline+C1D	Quiet	Quiet	FN	11h	13h	10h	Quiet	11h
Baseline	Quiet	Quiet	14h	9h	8h	4h	Quiet	8h
EarlyDetect	Quiet	Quiet	9h	5h	4h	1h	FP	4h
EarlyDetect+C1D	Quiet	Quiet	14h	8h	8h	2h	Quiet	8h
LSTM	Quiet	Quiet	14h	7h	8h	1h	Quiet	7h

Appendix C Continuum intensity forecast for the test active regions

Figures C1 through C4 illustrate the multi-model forecasts for the test active regions. These plots follow the same format as Figure 3 in the main text. Note: AR 11726 contains a period of missing data, appearing as a flat line in the forecast plots.

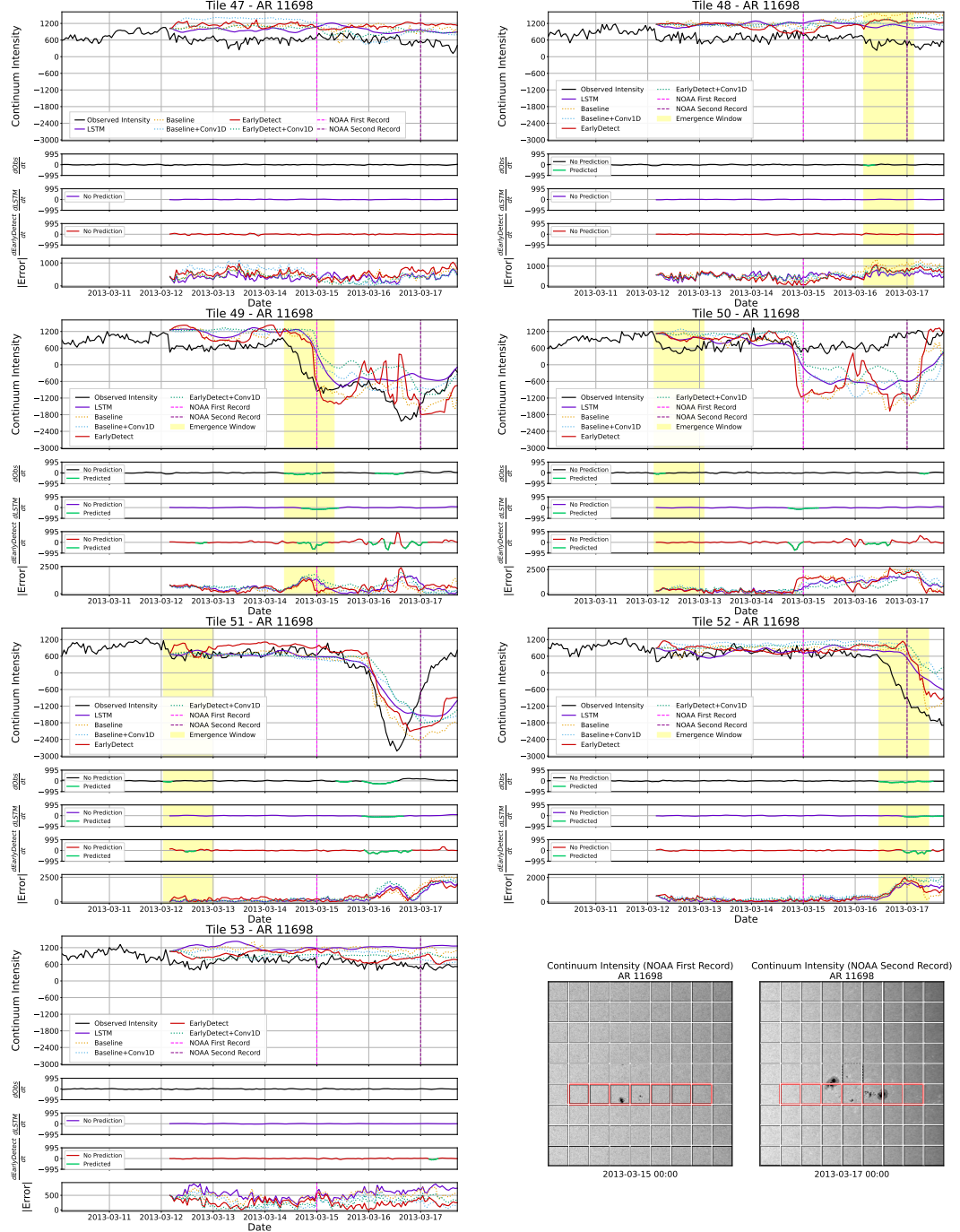


Figure C1: Comparison plot for AR 11698. This figure illustrates the high-variance behavior reported in Table B1. While the EarlyDetect model achieves a mean timing of -9.75h (early) on this active region, the visual forecast is volatile, characterized by sharp pre-emergence drops in specific tiles (e.g., Tile 49). The LSTM, while smoother, lacks this aggressive early sensitivity.

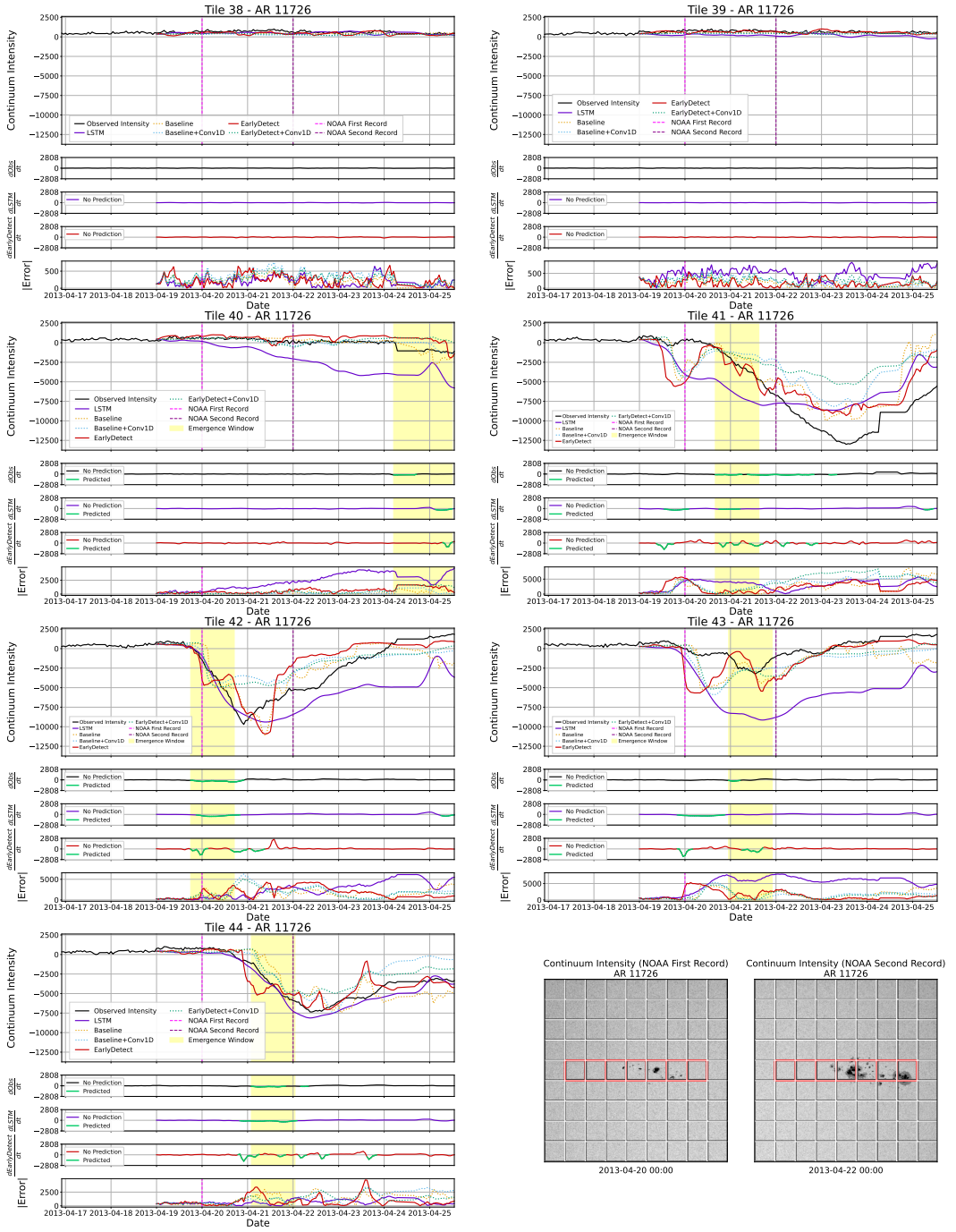


Figure C2: Comparison plot for AR 11726. This region represents a consistent success case for the Transformer architecture. The EarlyDetect predictions (red line) are visibly shifted to the left of the observed intensity drop (black line) across the active tiles, confirming the quantitative finding of a -9.40 hour mean advance warning. Note: This AR does have missing values in the data towards the end of the selected timeline, shown by the straight line from 4-24 to 4-25.

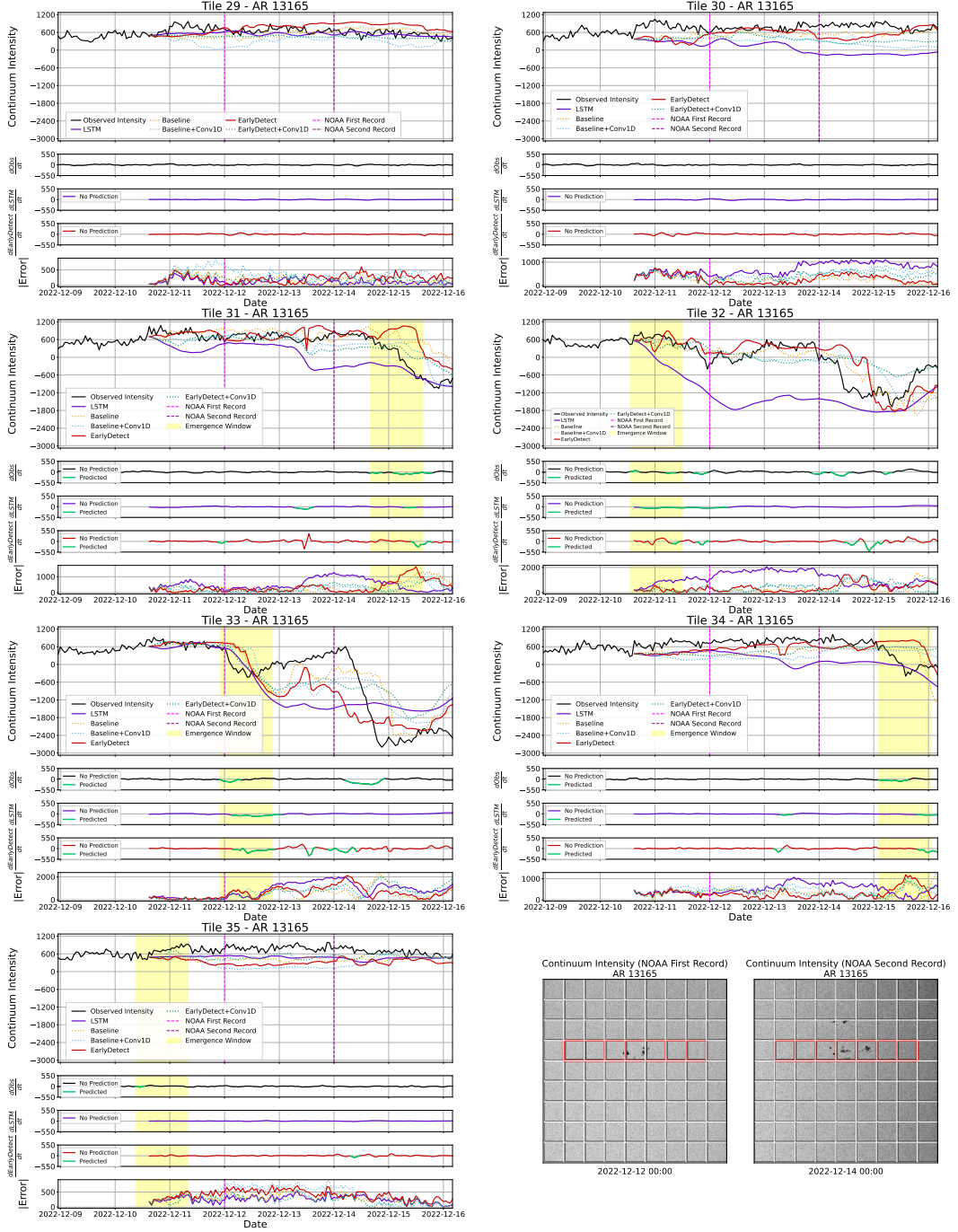


Figure C3: Comparison plot for AR 13165. This region exhibits the most significant advance warning capability of the EarlyDetect model. The characteristic “early dip” is clearly visible, particularly in Tile 31, where the model anticipates the emergence well in advance. This aggressive sensitivity drives the -26.25 hour mean timing difference reported in Table B3.

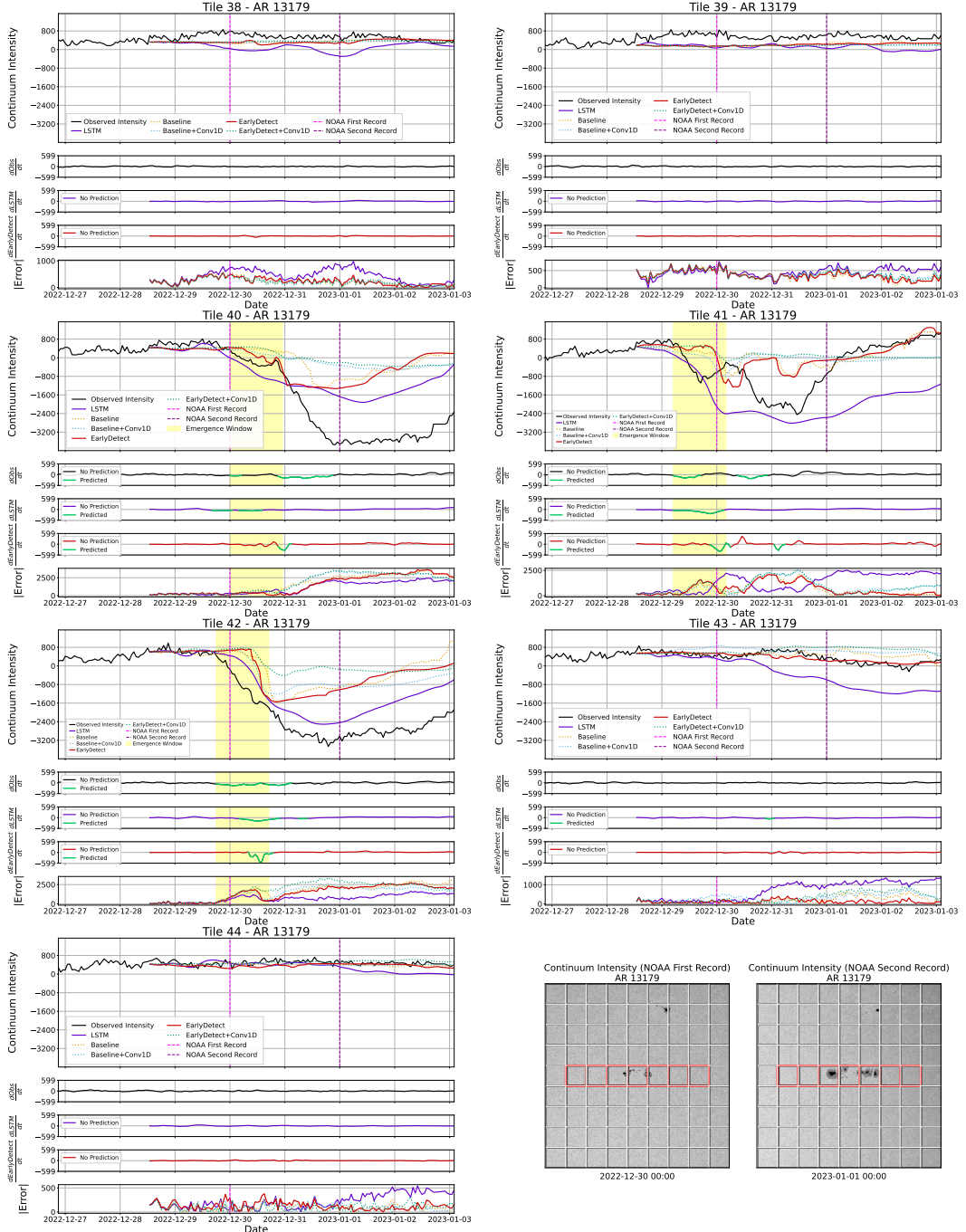


Figure C4: Comparison plot for AR 13179. This region represents a failure case for the attention-based models in the presence of shallow emergence signatures. The Transformer forecasts are visibly late, trailing the event by +17 hours, whereas the LSTM baseline (purple) maintains a closer alignment (+0.67h) to the observed emergence onset.